fluids

Article

Numerical Investigation of an Ocean Brick System

Hari Bollineni [1], Xiuling Wang [1,*] and Joshua Toblas [2]

[1] Mechanical and Civil Engineering Department, Purdue University Northwest, Hammond, IN 46323, USA
[2] Ocean Brick System Company, Mevo Beitar 99878, Israel
* Correspondence: wangx@pnw.edu

Abstract

A three-dimensional Computational Fluid Dynamics (CFD) model is developed to simulate an Ocean Brick System (OBS) placed in a wave tank. When stacked, ocean bricks are designed to withstand wave forces and ocean currents, enhancing the stability of offshore support structures, such as base supports of offshore wind turbines. In this study, the commercial software Ansys Fluent 2022 R1 is used for the simulations. A user-defined function (UDF) is developed to generate numerical waves that closely replicate those observed in experimental conditions. The numerical wave model is first validated against theoretical wave data, showing good agreement. The CFD model is then validated using experimental data from OBS tests conducted in the wave tank. Subsequently, the study investigates how OBS structures influence tidal waves—specifically, how they reduce the wave amplitude, and the pressure exerted on the bricks. Specifically, the wave amplitude reduction is more effective for waves with shorter wavelengths than for those with longer wavelengths, achieving up to a 70% reduction for waves with an amplitude of 0.785 m, a period of 5 s. Finally, a modification to the original brick geometry is proposed to further reduce wave amplitude and improve the stability of OBS platforms. For the same wave input, the modified brick geometry reduces wave energy effectively, achieving an 89.2% decrease in wave amplitude.

Keywords: numerical analysis; ocean brick system; wave amplitude reduction

check for updates

Academic Editor: Georgios Georgiou

Received: 7 July 2025
Revised: 22 August 2025
Accepted: 28 August 2025
Published: 1 September 2025

Citation: Bollineni, H.; Wang, X.; Toblas, J. Numerical Investigation of an Ocean Brick System. *Fluids* **2025**, *10*, 231. https://doi.org/10.3390/fluids10090231

1. Introduction

Rising sea levels from melting ice caps due to global warming poses severe threats to coastal regions. As water levels rise, coastal lines experience stronger wave activity and larger tidal surges. Increased wave energy leads to the erosion of beaches, dunes, and bluffs, as well as instability at the bases of offshore wind turbines. To address growing concerns related to rising sea levels, the OBS was developed [1]. OBS consists of an assembly of concrete modules, as shown in Figure 1a. When stacked, these modules serve various functions, including securing the foundations of offshore wind turbines and marinas as well as forming artificial reefs and large-scale port facilities. The mechanism diagram is shown in Figure 1b to illustrate the working mechanism of OBS. More importantly, OBS mitigates the force of incoming waves by dissipating wave energy, which reduces wave heights and ultimately limits erosion damage to offshore structures. As a base support for offshore wind turbines, the hollow structure of OBS also functions as a water reservoir, further enhancing its stability.

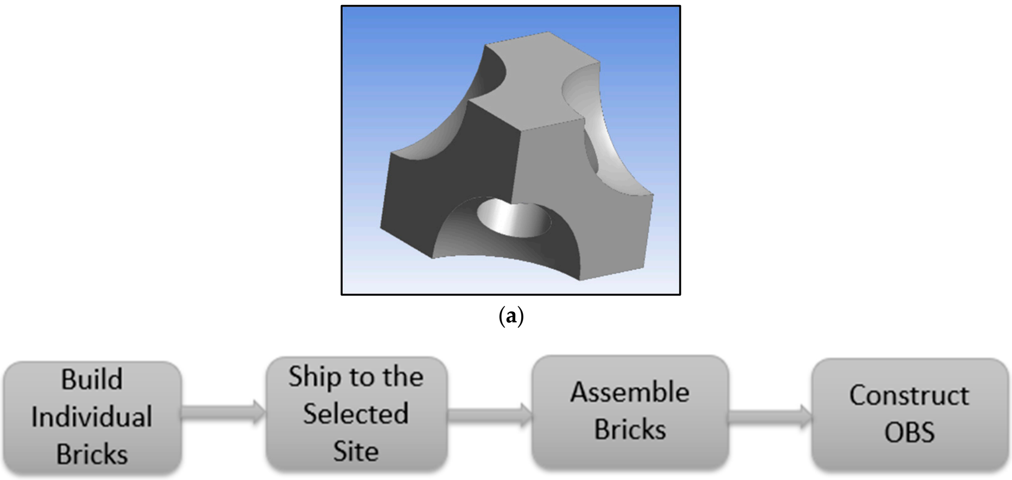

(**a**)

(**b**)

Figure 1. Ocean brick system (**a**) single brick (**b**) OBS workflow.

The objective of this study is first to validate the effectiveness of the OBS in dissipating wave energy and then to improve the structural stability of the system. Significant advancements in ocean wave simulation have been achieved, primarily through research involving wave tank experiments. A wave tank is a long, narrow container equipped with a wave generator at one end. Common wave generator designs include piston, flap, paddle, and wedge types, which are used to create controlled waves within the tank [2–4]. These traditional methods have led to important discoveries and insights, contributing to the development of offshore wind turbine foundations.

Setting up physical wave tanks presents several challenges. The financial cost of these facilities is substantial, and the space required to accommodate them further increases overall expenses. Additionally, constructing and testing prototypes is time-consuming. Early design iterations often do not guarantee success, potentially requiring redesigns and additional testing. Given these constraints, researchers have explored alternatives that maintain the quality and reliability of results. The simulation of OBS structures in Numerical Wave Tanks (NWTs) has emerged as a promising approach for cost-effective and efficient preliminary assessments, closely mirroring real-world conditions.

Many studies have investigated wave generation using a digital piston wave maker. Kim et al. programmed a wave maker to replicate the water movements at the edge of the wave generator, thereby creating fully three-dimensional waves [5,6]. The generated waves enter from one side by moving the water in sync with the wave maker. At the end of the tank, a damping zone was introduced to absorb the waves and reduce reflections. Similarly, Wang et al. [7] used a piston wave maker to generate the desired incident waves. Numerical methods were developed to solve Navier–Stokes equations with fully nonlinear boundary conditions for simulating the three-dimensional NWT. A finite analytical method was used to implement this model, enabling the analysis of wave generation and propagation. Gomes et al. [8] investigated regular gravity waves using two different numerical methods. They simulated wave generation via a wave function at the inlet and employed the Volume of Fluid (VOF) model to simulate wave propagation within the wave tank. Liang et al. [9] conducted simulations of a piston-type wave generator to produce a series of irregular waves. Using the Finite Volume Method (FVM), their simulation results were compared with experimental wave tank data, revealing strong consistency between the two.

Numerous techniques are available to simulate wave propagation. Li et al. [10] explored three distinct methods for modeling waves in two-phase CFD solvers: the Internal Wave Generator method, the Spectral Wave Explicit Navier–Stokes Equations method, and the Relaxation Zone method. The first two techniques generate and focus waves within a specific region, while the third enables viscous coupling throughout the entire domain. Separately, Choi et al. [11] investigated several common waves exit strategies during wave propagation in free surface simulations. They considered factors such as extended meshes, linear damping sources, increased viscosity, and wave reduction schemes. Their study compared the propagation of regular incident waves with the attenuation of radiative waves. Building upon existing techniques, Bihs et al. [12] developed a three-dimensional NWT to study wave propagation and wave loads. Their findings highlighted an improved density interpolation mechanism, which enhanced the accuracy of wave hydrodynamics simulations.

The value of these NWTs becomes evident when examining wave–structure interactions. Offshore structures, due to their constant exposure, must withstand and operate under relentless wave forces. Researchers have made significant advances in simulating these interactions using NWTs. For example, Kuai et al. [13] analyzed wave forces on cylindrical structures, highlighting the importance of vortex shedding behind these cylinders under wave impact. Kumar and Bhattacharjee [14] conducted a comprehensive study on breakwaters, focusing on the hydrodynamic performance and wave attenuation capabilities of seawalls. Using a two-dimensional NWT, they demonstrated that submerged breakwaters significantly reduce wave energy without obstructing shoreline views or access.

Leveraging the Reynolds-Averaged Navier–Stokes (RANS) equations coupled with the Renormalization Group (RNG) k-ε model, Yong and Mian [15] investigated a surface-piercing structure in a two-dimensional NWT. They revealed the complex effects of wave–current interactions on such structures, emphasizing the increased stresses experienced under simultaneous wave and current forces—an important consideration for structural design and maintenance. Hu et al. [16] used OpenFOAM to investigate wave-structure interactions, introducing a new wave theory to establish boundary conditions for modeling extreme wave scenarios. Subsequent studies have shown that wave energy decreases as it passes over permeable submerged breakwaters, shifting to higher frequencies and increasing turbulence near the water–structure interface [17]. Another study identified a relationship between draft and horizontal wave forces for regular waves impacting fixed truncated cylinders [18]. Akarni et al. [19] developed a numerical model using the Boundary Element Method (BEM) to analyze wave interactions with submerged plates, considering both linear and second-order wave theories. Similarly, Wang et al. [20] applied the Reynolds-Averaged Navier–Stokes (RANS) equations along with the k-ε turbulence model to evaluate wave loads on offshore bridge box-girder superstructures. Their results indicated that floating breakwaters significantly reduce the wave loads acting on such structures. They also developed a neural network-based model to predict maximum wave forces in the presence of floating breakwaters. Further, Tong et al. [21] introduced an enhanced numerical method—the Adaptive Harmonic Polynomial Cell (AHPC) Method—to improve simulations of 3D nonlinear wave–structure interactions involving embedded boundaries. Compared to standard BEM techniques, this method offers greater accuracy and efficiency while mitigating issues such as spurious oscillations in the computed forces.

Accurate and stable calculations are important when using NWTs. One of the major challenges in this context is achieving precise wave generation. The development and advancement of NWTs have significantly enhanced the understanding of the hydrodynamic behavior of structures and their interactions under various wave conditions. Even though there are lot of research on NWTs, to the best of authors knowledge, there is no literature has been published on CFD investigation of OBS. This research investigates the potential of an ocean brick structure within NWTs using the commercial software Ansys Fluent.

Follow by the second-order Stokes waves theory, numerical investigations were conducted under different wave conditions (wave amplitude, period**,** and wave length) for both linear and nonlinear "depth" NWTs. First, the Volume of Fluid (VOF) model is used to generate waves in both linear and nonlinear NWTs, and the results are validated against analytical solutions to ensure accuracy. Subsequently, the interaction between waves and the OBS model is studied within an NWT that replicates an experimental setup. The simulation uses real-world dimensions, resulting in a more realistic representation. The generated wave is validated using an analytical solution, the simulation results in the nonlinear NWT with the OBS are compared against experimental data. Based on the findings, a modified brick geometry is proposed. This modified OBS design shows greater potential to reduce wave energy and enhance structural stability, making it a more effective support system for offshore wind turbines.

2. Numerical Methods

2.1. Porous Medium

Many offshore and coastal structures benefit from the use of porous surfaces, which provide additional resistance to wave forces. Coarse gravel beds are a prime example; they allow water to flow through while offering a stable foundation for structures such as piers and jetties. These porous layers help dissipate wave energy, reducing erosion and enhancing the stability of the structure. Such design choices play a critical role in creating durable and resilient coastal infrastructure.

The parameter ε represents the porosity of a porous medium, which is a ratio of the volume of void V_ν to the total volume V_0, $\varepsilon = \frac{V_\nu}{V_0}$.

A complete solid structure would possess a porosity of 0, indicating no voids. While a volume comprised entirely of voids would have a porosity of 1. The residual component V_s of the porous medium, which is not occupied by voids, constitutes the "skeletal" structure of the material, $V_\nu + V_s = V_0$.

The porosity of a medium is determined by its relationship with density: $\varepsilon = 1 - \frac{\rho_\Sigma}{\rho_0}$, where $\rho_\sum$ is porous medium density and ρ_0 is the density of material forming its skeleton.

Various models have been formulated to elucidate the dynamics of flow through porous media and compute the associated pressure drop as fluids traverse these mediums. Often, these mathematical representations derive from empirical observations and findings.

Darcy pioneered a unidimensional empirical approach to characterize laminar flow within porous media [22].

$$-\nabla p^* = \frac{\mu}{\alpha}\mu^* \tag{1}$$

where μ^* represent the flux per unit area, α denote the permeability, μ be the dynamic viscosity and Δp stands for the pressure gradient in the flow direction. Darcy's law is conventionally employed to articulate fluid movement in porous media that are microscopically disordered yet macroscopically homogeneous [23]. Darcy's formulation does not consider inertial effects. Its applicability is primarily restricted to flows exhibiting low Reynolds numbers.

For turbulent flow within porous media, one must account for both viscous and inertial effects, as they induce more intricate nonlinear patterns in the flow behavior. Recognizing this complexity, Forchheimer introduced an additional term to Darcy's original formulation, ensuring that this nonlinearity was duly considered. Forchheimer's equation is widely acknowledged as the evolved extension of Darcy's law, specifically tailored for scenarios with elevated flow rates. The Forchheimer equation is expressed in Equation (5) [24].

$$-\nabla p^* = \frac{\mu}{\alpha}\mu^* + \beta\rho\mu^{*2} \tag{2}$$

where β is the non-Darcy coefficient.

Two different porous media used to support the OBS are simulated using the porous media model. As wave-induced flow develops at the bottom of the tank, it passes through these porous layers, which offer partial resistance due to increased viscous and inertial effects. These effects contribute to the development of turbulence in the flow direction near the porous media. This resistance generates a back pressure in the flow, which is calculated using the Forchheimer equation, as previously described.

2.2. Generation of Numerical Waves

The propagation of waves is facilitated by a user-defined function to generate a wave on the left end within the NWT. In this study, the velocity components are determined using the second-order Stokes wave theory. Stoke's second-order wave theory is a form of a linear wave theory with an additional higher-order term.

As per Horko [25], the motion of free surface elevation η in the Stokes theory can be written as:

$$\eta = Acos(Kx - \omega t) + \frac{A^2K(\cosh(KH))}{4sinh^3(KH)}(2 + cosh(2KH))cos2(Kx - \omega t) \tag{3}$$

The velocity components in x and z direction can be expressed as:

$$u = \frac{AgKcosh(Kz)}{\omega cosh(KH)}cos(Kx - \omega t) + \frac{A^2\omega K\ cosh(2Kz)}{sinh^4(KH)}cos(2(Kx - \omega t)) \tag{4}$$

$$w = \frac{AgKsinh(Kz)}{\omega sinh(KH)}sin(Kx - \omega t) + \frac{A^2\omega K\ sinh(2Kz)}{cosh^4(KH)}sin(2(Kx - \omega t)) \tag{5}$$

where $K = \frac{2\pi}{L}$ is the wave number, $\omega = \frac{2\pi}{T}$ is the wave frequency, z is the change in position in the free water surface to the sea floor, A is the amplitude of the wave, T is the time period, L is the wavelength, and H is the water depth.

Wavelength is calculated using Equation (6) [26] based on water depth and time period. The generated wavelength in NWT is independent of wave height.

$$L = \frac{gT^2}{2\pi}tanh(\frac{2\pi H}{L}) \tag{6}$$

2.3. VOF Model

In the NWT, the Volume of Fluid (VOF) model is employed to capture water–air interactions [27]. The VOF model is specifically designed for immiscible fluids, meaning fluids that cannot mix. It simulates the behavior of these distinct fluids using a shared set of momentum equations while tracking the volume fraction of each fluid within a computational cell. Its ability to maintain clear phase separation makes it a valuable tool for studying interactions between immiscible fluids in dynamic environments.

In VOF model, each fluid's movement is tracked using a volume fraction variable, which indicates the portion of a computational cell occupied by a specific fluid. The volume fraction of air or water in each cell is represented by α_a (α_w) and the possibilities:

$\alpha_a = 0$: Devoid from air.

$\alpha_a = 1$: Filled with air.

$0 < \alpha_a < 1$: Partially filled with water and air. Since the mixture is filled with only air and water, so $\alpha_a + \alpha_w = 1$.

To monitor the interface between two phases, the continuity equation is solved for the phase volume fractions:

$$\frac{1}{\rho_a}\left(\frac{\partial}{\partial t}\alpha_a\rho_a + \nabla\bullet\alpha_a\rho_a v_a\right) = S\alpha_a + \sum(m_{aw} - m_{wa}) \tag{7}$$

$$\frac{1}{\rho_w}\left(\frac{\partial}{\partial t}\alpha_w\rho_w + \nabla\bullet\alpha_w\rho_w v_w\right) = S\alpha_w + \sum(m_{wa} - m_{aw}) \tag{8}$$

Here, m_{aw} represents a transfer of mass from air to water, and m_{wa} denotes the transfer of mass from water to air. $S\alpha_a$ and $S\alpha_w$ are typically assumed to be zero and can also represent a continuous or user-defined mass source for every phase. To determine the velocity field across the entire domain, the momentum equation is defined using each phase's characteristics, such as density (ρ) and viscosity (μ) shown in Equations (9) and (10).

$$\frac{\partial}{\partial t}\rho_a v + \nabla\bullet\rho_a v\, v = -\nabla P + \nabla\bullet(\mu_a(\nabla v + \nabla v^T)) + \rho_a g + F \tag{9}$$

$$\frac{\partial}{\partial t}\rho_w v + \nabla\bullet\rho_w v\, v = -\nabla P + \nabla\bullet(\mu_w(\nabla v + \nabla v^T)) + \rho_w g + F \tag{10}$$

Shared field calculation does have its drawbacks. For starters, when there is a significant difference in the speeds of two phases, it might not be very accurate, especially near the boundary where the two meet. Additionally, it can struggle to capture tiny details or rapid changes at these interfaces.

2.4. Turbulence Model

The Shear Stress Transport (SST) k-omega turbulence is employed due to its ability to accurately model both near-wall and free flow. It is a combination of the k-omega near the wall and the k-epsilon for free flow, providing a seamless transition between the two regions [28]. This combination allows the model to effectively capture complex flow structure interactions, especially when dealing with free surface flows and wave generation.

The SST k-ω model is governed by Equations (11) and (12).

Turbulent kinetic energy (k) equation:

$$\frac{\partial\rho k}{\partial t} + \frac{\partial\rho k u_i}{\partial x_i} = \frac{\partial}{\partial x_j}\left((\mu + \sigma_k\mu_t) + \frac{\partial k}{\partial j}\right) + G_k + G_b - \rho\beta^* k_\omega + S_k \tag{11}$$

Specific dissipation rate (ω) equation:

$$\frac{\partial\rho\omega}{\partial t} + \frac{\partial\rho\omega u_i}{\partial x_i} = \frac{\partial}{\partial x_j}\left((\mu + \sigma_\omega\mu_t) + \frac{\partial\omega}{\partial x_j}\right) + \frac{\alpha\omega^2}{v_t}\left(G_k + \frac{G_b}{C_\mu}\right) - \rho\beta\omega^2 + S_\omega \tag{12}$$

where ρ is the density of fluid, x_i and x_j are spatial coordinates, u_i is velocity in xi direction, t is time, μ is viscosity, μ_t is eddy viscosity, G_k, G_b are the production of turbulent kinetic energy due to mean velocity gradients and buoyancy, respectively, S_k, S_ω are user-defined source terms, and the model constants α, β, β^*, σ_k, and σ_ω are derived from experimental data and empirical correlations [28].

3. Model Setup and Validation

Simulations are first conducted in a linear-depth NWT as a baseline case. The resulting surface elevations are compared with analytical solutions for validation purposes. Numerical analyses are then performed in a nonlinear-depth NWT, both with and without an OBS, and the wave amplitudes are collected to evaluate the brick's effectiveness in reducing wave energy. To verify the model's accuracy, pressure data from eight locations are extracted from the simulation results, and are compared with corresponding experimental data. Finally, a modified brick design is proposed, and simulation results using the modified brick are compared with those from the traditional design to assess its effectiveness in wave energy reduction.

3.1. Model Setup and Boundary Conditions

3.1.1. Linear Depth NWT

A NWT with dimensions of 25 m in length, 3 m in width, and 1.5 m in depth is used in the simulation. Detailed boundary settings are given in Figure 2. The front, back, and bottom walls are considered as no-slip boundary conditions, indicating that the fluid velocity at the interface with these solid surfaces is zero [29]. The left boundary of the computational domain is set as a velocity inlet with wave inflow applied through a UDF. The right end of the NWT is defined as a pressure outlet; the top boundary is specified as a pressure inlet open to the atmosphere

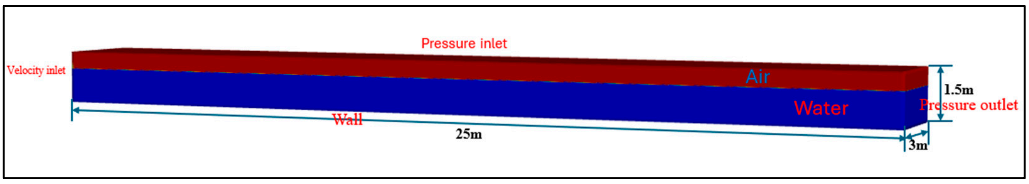

Figure 2. Three-dimensional NWT for validation.

A structured grid is utilized for meshing, with an element size of 0.1 m. To accurately capture free surface interactions, the mesh is refined around the interface. The total number of cells in the NWT is 656,500, and is shown in Figure 3.

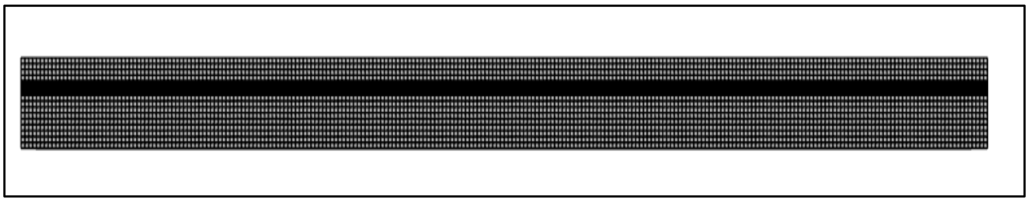

Figure 3. Three-dimensional NWT meshes.

3.1.2. Nonlinear Depth NWT

The nonlinear depth NWT of the length has a length of 321.24 m, a width of 40 m, and an initial depth of 6.81 m. The depth varies nonlinearly based on the equation $-0.0047x^4 + 0.1061x^3 - 0.7717x^2 + 1.4198x + 6.1129$, which defines the sea bottom profile shown in Figure 4a. This configuration matches the experimental setup. A structured grid is used for meshing, with a base element size of 0.75 m, the grid is refined 1 m above and below the water surface to accurately capture the free surface interactions. In this region, the mesh is progressively refined using a ratio of 1.05, as illustrated in Figure 4.

The OBS experimental setup consists of 20 bricks arranged in two rows and 10 columns. Each brick measures 4 m × 4 m × 4 m and is placed on two underlying layers: a main rock bed and a rice grain bed, with porosity of 0.47 and 0.40, respectively. The Main rock bed is located at the bottom, with a rice grain bed positioned above it. The bricks are arranged on top of these layers to represent real-life base support system on the seashore, as shown in Figure 5.

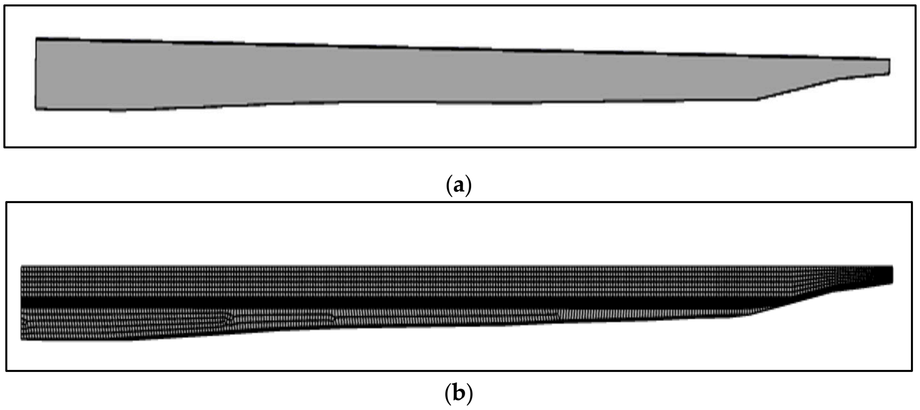
(**a**)

(**b**)

Figure 4. (**a**) NWT with nonlinear depth and (**b**) NWT with mesh.

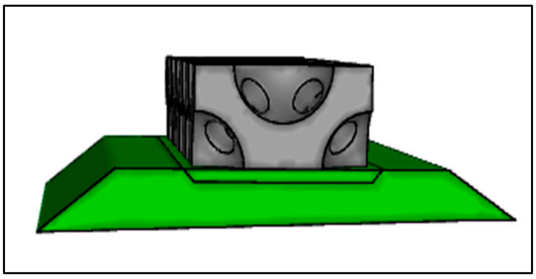
Figure 5. Ocean brick arrangement on a main rock bed.

The entire OBS is placed 87 m from the inlet in the nonlinear depth NWT as shown in Figure 6.

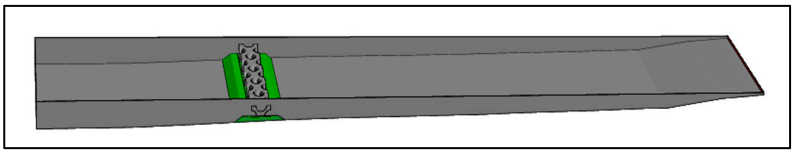
Figure 6. NWT with OBS.

Each brick was submerged to a height of 2.9 m from its bottom, with the origin positioned transversally at the center of the brick arrangement, measured from the base of the brick. In the experimental setup, pressure sensors were mounted at eight different locations, as shown in Table 1.

Table 1. Experimental Pressure Locations.

Pressure	Location (x, y, z) (m)
P1	−4.0, 13.32, 2.68
P2	−4.0, 14.32, 1.68
P3	−4.0, 15.28, 0.72
P4	4.0, −13.32, 2.68
P5	4.0, −14.32, 1.68
P6	4.0, −15.28, 0.72
P7	2.0, −10.0, 0.00
P8	−2.0, −10.0, 0.00

3.2. Mesh Independent Study

A mesh independent study is conducted using different element sizes, as shown in Table 2. Multiple simulation trials confirm that the results remain consistent regardless of mesh size.

Table 2. Mesh Size and Cell Count.

Mesh Set #	Element Size (m)	Cell Count
1	1.25	134,400
2	1.00	228,920
3	0.75	477,522
4	0.65	728,810
5	0.50	1,462,880

All mesh sets are tested using constant wave parameters: A = 0.785 m and T = 4 s. The wave generator is employed to reproduce wave propagation, with the incident velocity defined using a UDF based on Stokes' second-order wave theory. Data is collected at x = 25 m, where free surface elevations are recorded without placing OBS in NWT, as shown in Figure 7.

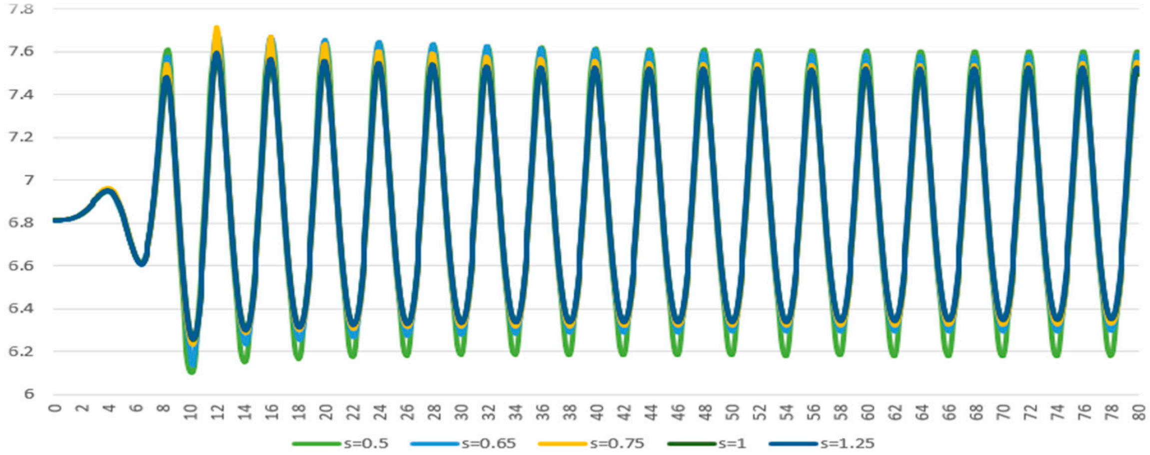

Figure 7. Surface elevation for different element sizes.

Free surface wave amplitudes are recorded after the wave stabilizes in the NWT. The measured average amplitudes for each element size are presented in Table 3 and compared with the analytical amplitude of 0.77 m. The mesh size of 1.25 m yields the largest error at 23.32% while the 0.5 m mesh produces the smallest error at 6.39%.

Table 3. Numerical Wave Amplitude Compared with Analytical Value.

Element Size (m)	Wave Amplitude (m)	% Error
1.25	0.59	23.32
1.00	0.60	22.00
0.75	0.63	18.12
0.65	0.67	12.95
0.50	0.72	6.39

For the element size of 0.5 m, the mesh count is 1,462,880, which is relatively high and significantly increases the computational cost. Introducing the OBS into the tank further increases both the mesh count and computational cost substantially.

To maintain optimal performance by keeping mesh count and computational cost reasonable, it is important to improve the mesh quality at the air-water interface. For this purpose, the mesh is refined in a region extending one meter above and one meter below the interface. Within this zone, the grid is progressively refined using a ratio of 1.05. An element size of 0.75 m is used in the simulation. Surface elevation data at location x = 25 m in the NWT is collected and compared for mesh element sizes of 0.5 and 0.75 without mesh refinement. The results are shown in Figure 8 for the same location.

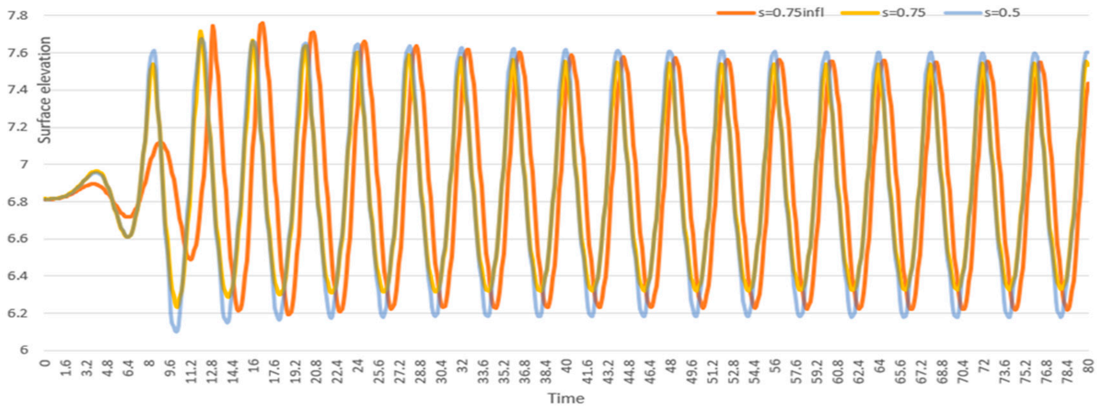

Figure 8. Surface elevation for different mesh refinements.

Data is collected after the wave gets stabilized in the NWT. The difference in mesh count and wave amplitude error, compared to the analytical value of 0.77 m, are presented in Table 4. When comparing the mesh size of 0.5 m and 0.75 m with interface refinement, the mesh count is reduced by 465,300, with only a 0.3% difference in wave amplitude. This result indicates that mesh refinement at the interface significantly improves computational accuracy while reducing the overall mesh size.

Table 4. Amplitude Comparison from Various Mesh Sizes with Analytical Value (0.77 m).

Element Size (m)	Cell Count	Amplitude (A) (m)	% Error
0.5	1,462,880	0.72	6.39
0.75	477,522	0.63	18.12
0.75 with refinement	997,580	0.71	6.73

The mesh size of 0.75 with refinement at the air-water interface is chosen to further study the wave interaction with OBS in NWT. The entire NWT model is meshed using hexahedral elements. Additional mesh refinement is applied around the structure by introducing tetrahedral elements near the OBS and porous beds to capture enhanced detail, as shown in Figure 9. Consequently, the total mesh count increases to 1,550,000 cells.

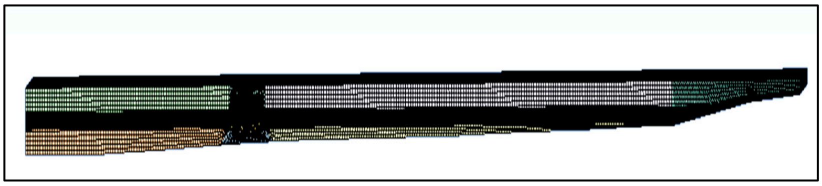

Figure 9. Overall mesh with OBS in NWT.

Tetrahedral elements with size 0.1 m are chosen for the mesh zone surrounding the OBS and porous medium, as shown in Figure 10a. The capture curvature feature is applied with a minimum element size of 0.02 m to better approximate the spherical and conical regions near the bricks. The flow adjacent to a wall surface forms a boundary characterized by velocity gradients dominated by viscous effects. The y+ value indicates the relative importance of viscous forces within the boundary flow sublayer and the turbulence effects. The y+ value is expected to be within the 50–500 range to accurately capture boundary flow for the SST k-omega model. The current mesh achieves a y+ value of 259 in the wake zone near the OBS and porous region. To maintain an appropriate y+ value, the mesh gradually transitions from larger to smaller elements, as illustrated in the cross-sectional interface between the OBS and water in Figure 10b.

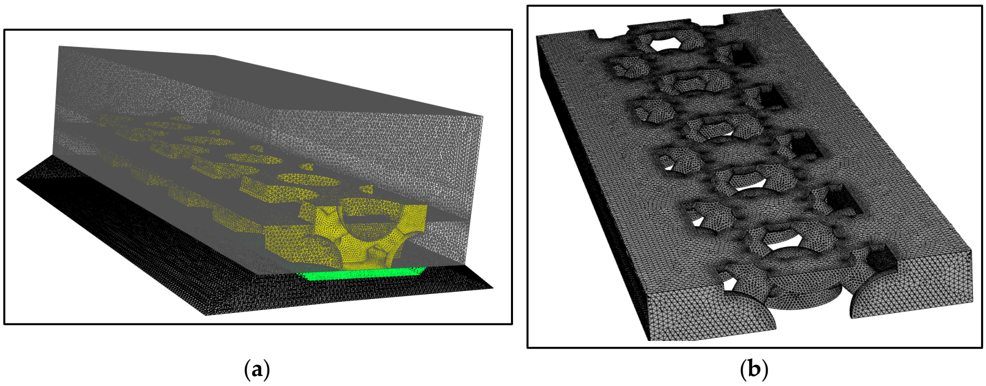
(**a**) (**b**)

Figure 10. Close view of NWT mesh (**a**) around the OBS and porous medium (**b**) cross-section of OBS.

3.3. Validation

Firstly, validation is conducted in the linear depth NWT using a wavelength of 3.51 m, wave amplitude of 0.1 m, time-period of 2 s, and a still water depth (free surface) of 1 m.

In Figure 11, the blue-colored region signifies water, while the red-colored region indicates air. Figure 11 illustrates wave propagation at various time steps.


(**a**) t = 0 s


(**b**) t = 5 s


(**c**) t = 10 s


(**d**) t = 15 s


(**e**) t = 20 s

Figure 11. Wave propagation in NWT over various time periods.

To validate the current numerical setup for simulating intermediate-depth gravity waves, the free surface elevation in the NWT is compared with the analytical solution, please refer to Equation (6), based on Stokes second order wave theory [25].

Figure 12a shows the free surface elevation of numerical wave collected at x = 5 m for wave characteristics of A = 0.1 m and T = 2 s in linear depth NWT. Figure 12b presents data collected at x = 25 m for wave characteristics A = 0.785 m and T = 4 s in nonlinear depth NWT. In both cases, the free surface elevations were recorded without introducing the OBS into the NWT.

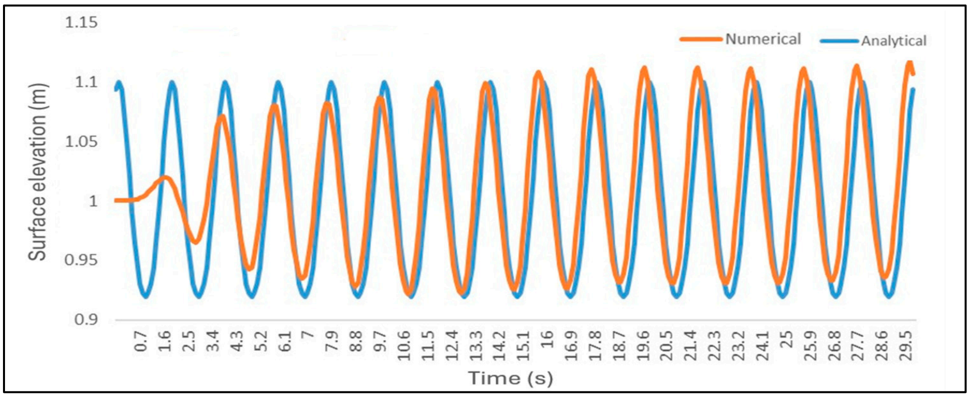

(**a**) x = 5 m linear depth NWT

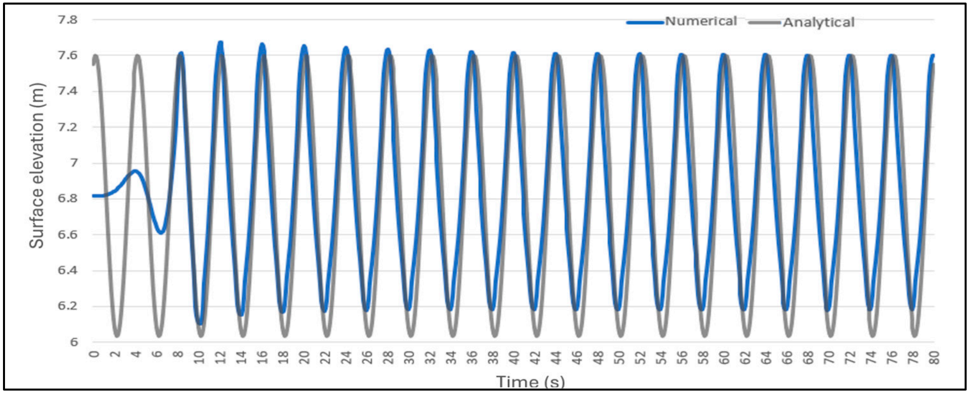

(**b**) x = 25 m in nonlinear depth NWT

Figure 12. Wave heights comparison between simulation and analytical results.

At first, the free surface elevations produced in both NWTs are lower than those predicted by the analytical solution. However, after a certain period, the wave profiles stabilize and align with the numerical results, though some elevation is observed near the end of the tank due to wave reflections. In both cases, the analytical wave amplitude differs by approximately 0.05 m from the average numerical wave amplitude after stabilization. The percentage error difference is 6% for nonlinear NWT and 5% for linear NWT. These validation results confirm the effectiveness of the simulated numerical wave approach in generating intermediate gravity waves based on the Stokes second-order wave theory.

4. Results

4.1. Numerical Results with Original Brick

Numerical simulations are performed with the OBS in the nonlinear-depth NWT using different wave parameters, as shown in Table 5, and results are validated against experimental data. The wavelength conditions are calculated using the wave period (T) in seconds, the initial water depth (H) of 6.8126 m, and the wave amplitude (A) in meters, as defined by Equation (6). A transient simulation was conducted for 80 s without a damping zone to analyze the interaction between the simulated wave and the OBS under various wave parameters.

Table 5. Simulation Cases.

Case No.	Time Period(t) (s)	Wave Amplitude(A) (m)
1	4	0.785
2	5	0.770
3	6	0.735
4	7	0.755

The wavelength conditions are calculated using the wave period (T) in seconds, the initial water depth (H) of 6.8126 m, and the wave amplitude (A) in meters, as defined by Equation (6). A transient simulation was conducted for 80 s without a damping zone to analyze the interaction between the simulated wave and the OBS under various wave parameters.

As shown in Figure 13, which compares simulation results for the four cases (with/without OBS), the OBS effectively mitigates the wave's impact by dissipating wave energy. After passing the OBS, the water level behind the structure remains relatively stable, with only minor fluctuations. This analysis demonstrates the OBS's ability to manage ocean waves and protect areas behind the structure from significant wave-induced disturbances.

(**a**) Case 1 (A = 0.785 m, T = 4 s) with brick.

(**b**) Case 1 (A = 0.785 m, T = 4 s) without brick.

(**c**) Case 2 (A = 0.770 m, T = 5 s) with brick.

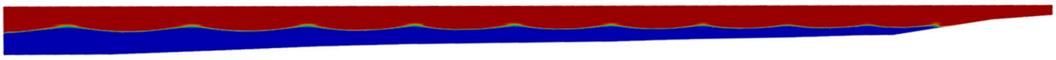

(**d**) Case 2 (A = 0.770 m, T = 5 s) without brick.

(**e**) Case 3 (A = 0.735 m, T = 6 s) with brick.

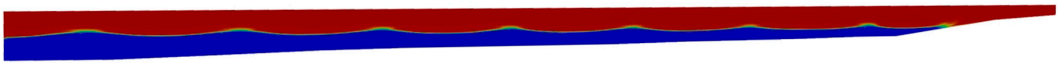

(**f**) Case 3 (A = 0.735 m, T = 6 s) without brick.

(**g**) Case 4 (A = 0.755 m, T = 7 s) with brick.

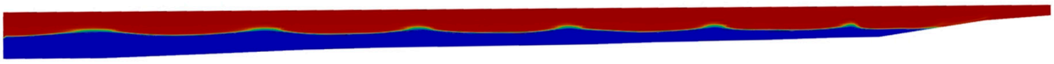

(**h**) Case 4 (A = 0.755 m, T = 7 s) without brick.

Figure 13. Wave propagation through the NWT with and without OBS.

To evaluate the wave-brick interactions, the water surface elevation is tracked at two locations: 5 m in front of the brick and 5 m behind it. As shown in Figure 13a–d for shorter wavelengths (Case 1 and 2), the compounding effects between subsequent waves are negligible, and the brick dissipates the wave energy effectively. In contrast, for longer wavelengths (Case 3 and 4), wave interactions become more complex as subsequent waves collide and interfere with one another. As a result, the OBS bricks are less effective at quickly dissipating the wave quickly, as shown in Figure 13e–h.

The primary function of the OBS is to reduce the incoming wave amplitude by dissipating wave energy. OBS effectiveness is quantified as the difference in wave amplitude compared to the condition without the brick structure. As shown in Table 6, it is clear that the OBS is effective for shorter wavelengths—for example, in case 1, where L = 23.67 m, which corresponds to lower-energy waves, the wave amplitude reduction is 70.8%. In contrast, for longer wavelengths such as in Case 4 (L = 51.86 m), the effectiveness of the OBS decreases to 45.4%. In this case, the amplitude of the incident wave is nearly twice that of the wave after passing over the OBS, as illustrated in Figure 14.

Table 6. Wave Amplitude Comparison of Brick with No Brick at x = 5 m Behind the Structure.

Case No.	Wave Amplitude Reduction%
1	70.8
2	68.2
3	63.5
4	45.4

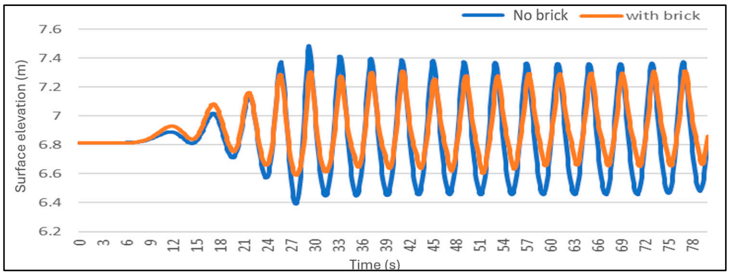

(**a**) Case 1, 5 m in front of brick.

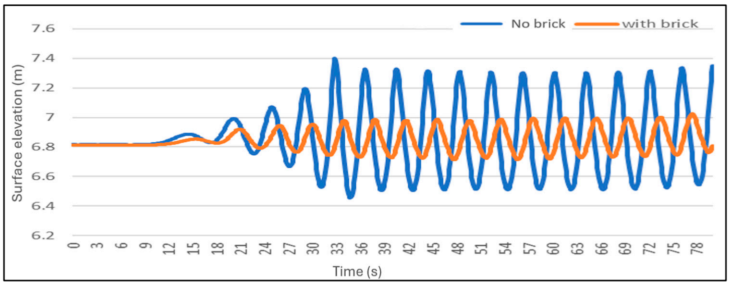

(**b**) Case 1, 5 m behind the brick.

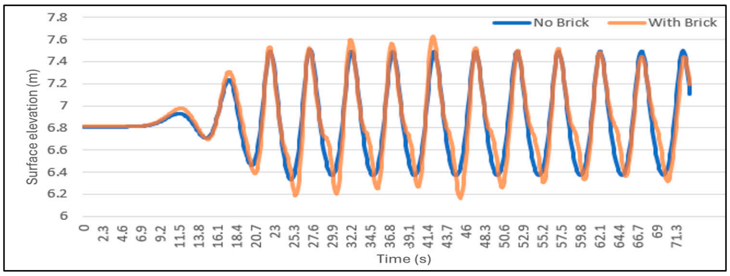

(**c**) Case 2, 5 m in front of brick.

Figure 14. *Cont.*

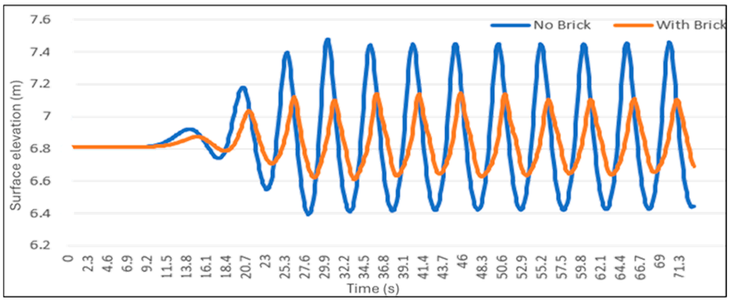

(**d**) Case 2, 5 m behind the brick.

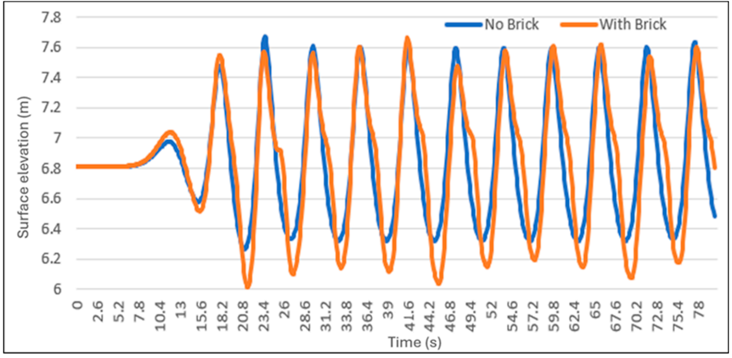

(**e**) Case 3, 5 m in front of brick.

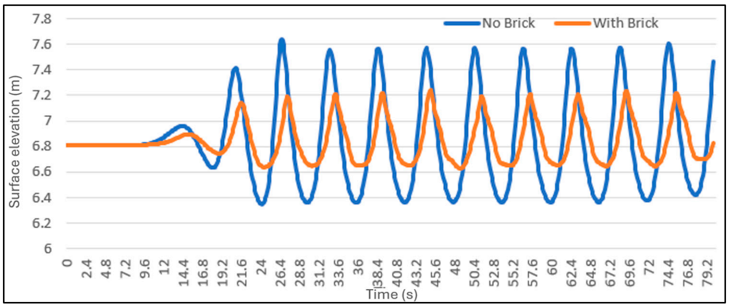

(**f**) Case 3, 5 m behind the brick.

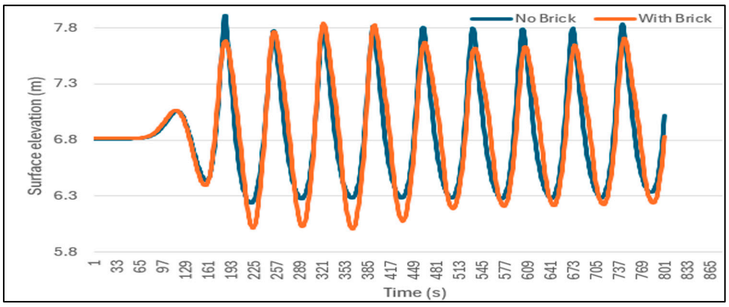

(**g**) Case 4, 5 m in front of brick.

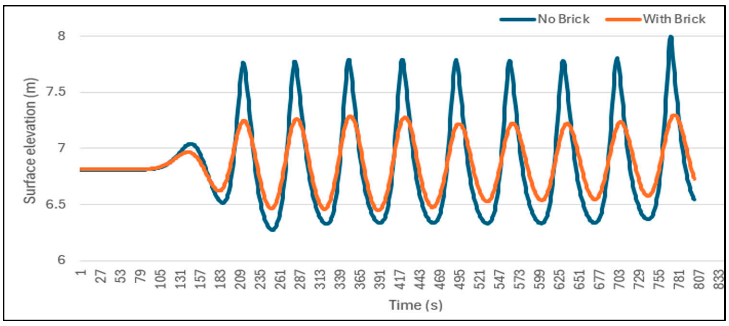

(**h**) Case 4, 5 m behind the brick.

Figure 14. Surface elevations at 5 m in front and behind the brick for different wave parameters.

To assess the impact of OBS on ocean waves, experiments were conducted by the manufacturer of OBS—the Ocean Brick Technology. Pressure readings were taken at eight distinct locations, as outlined in Table 7. Points P1, P2, and P3 are situated on the side facing the incoming wave, while points P4, P5, and P6 are located on the opposite side, away from direct wave impact. Points P7 and P8 are positioned on the underside of the OBS structure. These pressure measurements data are provided by the Ocean Brick Technology. Pressure values from both the current simulation and the provided experiments data were recorded at the same respective locations.

Table 7. Comparison of Pressure Between Simulation and Experiment.

(**a**) Case 1 A = 0.785 m and T = 4 s			
Pressure	**Exp (Kpa)**	**Simulation (Kpa)**	**Error %**
p1	10.00	8.62	13.80
p2	8.40	7.65	8.93
p3	7.70	7.19	6.62
p4	2.30	2.94	27.82
p5	2.20	2.71	23.18
p6	2.20	2.66	20.9
p7	5.80	4.84	16.55
p8	1.90	3.05	60.52
(**b**) Case 2 A = 0.77 m and T = 5 s			
Pressure	**Exp (Kpa)**	**Simulation (Kpa)**	**Error %**
p1	10.00	8.62	13.80
p2	8.40	7.65	8.93
p3	7.70	7.19	6.62
p4	2.30	2.94	27.82
p5	2.20	2.71	23.18
p6	2.20	2.66	20.90
p7	5.80	4.84	16.55
p8	1.90	3.05	60.52
(**c**) Case 3 A = 0.77 m and T = 5 s			
Pressure	**Exp (Kpa)**	**Simulation (Kpa)**	**Error %**
p1	11.50	10.96	4.69
p2	11.60	10.51	9.39
p3	9.30	9.32	0.21
p4	3.60	3.07	14.72
p5	2.90	2.70	6.89
p6	2.90	2.6	10.34
p7	3.80	3.86	1.57
p8	6.60	6.16	6.66

Table 7. *Cont.*

(**d**) Case 4 A = 0.755 m and T = 7 s			
Pressure	**Exp (Kpa)**	**Simulation (Kpa)**	**Error %**
p1	14.70	14.61	0.61
p2	13.00	13.83	6.38
p3	12.90	12.81	0.69
p4	5.20	5.32	2.30
p5	4.50	4.73	5.11
p6	4.10	3.86	5.85
p7	5.20	5.91	13.65
p8	9.80	9.67	1.32

The pressure values measured at the specified locations are generally consistent with the experimental data provided by the OBS manufacturer, indicating the model's accuracy in capturing wave-induced pressure. However, the pressure values show deviations from the experimental results, likely due to the complex wave motion within the brick arrangement and the subsequent flow interactions on the backside of the structure.

Due to wave impact, the points on the wave-facing side exhibit the highest pressure, while the points on the opposite side show the lowest pressure, as a result of the dissipated wave passing through-consistent in both the simulated and experimental data. This analysis highlights that the OBS effectively dissipates wave energy for shorter wavelengths but requires further improvements to enhance energy dissipation for longer wavelengths.

4.2. Numerical Results with Modified Brick

4.2.1. Modified Brick Geometry

Threads inside tubes cause helical flow paths, inducing a swirling motion in the fluid as it passes through [30]. The internal threads can both guide and disrupt the fluid motion. According to Helmholtz's vortex theorem, this swirling motion persists along the tube unless acted upon by external forces [31]. However, spiraling flow introduces disturbances and turbulence into the fluid, leading to increased head losses (i.e., energy losses). Increasing the number of internal threads results in higher energy consumption for fluid flow [30].

Nozzles that manipulate the cross-sectional area of a flow alter fluid velocity and generate pressure variations. When a fluid enters a contraction region, its velocity increases while static pressure decreases. Conversely, in an expansion region, the velocity decreases and static pressure rises. An optimal combination of contraction ratio and convergence angle helps maintain a continuous velocity profile and prevents abrupt pressure changes.

Based on the findings discussed above, incorporating threaded and nozzle features into the brick design may effectively reduce the energy carried by incoming waves.

The brick structure is modified only along the internal tunnels to maintain its overall structural integrity (see Figure 15). The two tunnel sizes on the side of the incoming wave are enlarged to 1.8 m to capture more wave energy, while the remaining two tunnels are kept at 1.6 m and 1.4 m, respectively. The drill holes are tapered to form converging diverging nozzles, which generate back pressure to resist incoming waves at each time step. Threading is introduced along these tapered tunnels, causing the water to swirl, as illustrated in Figure 16. The taper helix method is used in SolidWorks 2024 while generate the modified geometry. For the thread, the height is 0.9 m, pitch is 0.25 m taper helix angle is 11.50 degree. The thread surface mesh size is 0.13 m. The swirling motions from opposite directions collides at the center of the brick, effectively dissipating the wave energy.

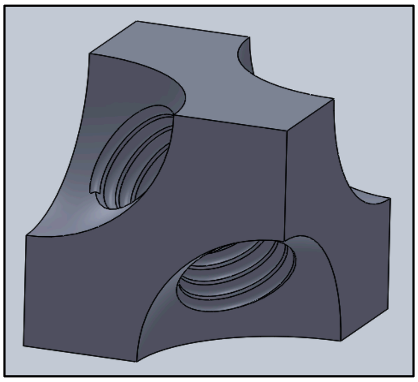

Figure 15. Modified Ocean brick.

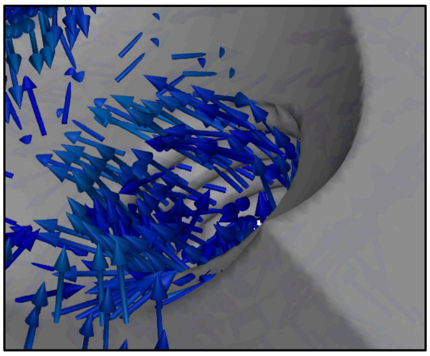

Figure 16. Velocity vector on the thread surface of the modified brick.

4.2.2. Simulation Results with Modified Brick

Simulation is carried out in the same nonlinear depth NWT by replacing the traditional brick with a modified brick geometry. Surface elevation and pressure data are collected at the same locations as traditional brick for cases 1 (shorter wave length) and case 4 (longer wave length), Results are then compared to assess the effectiveness of the modified brick geometry, there are about 30 points per thread.

Wave interactions with modified brick for cases 1 and 4 are shown in Figure 17, the surface elevation behind the brick for case 1 appears relatively still, whereas in case 4, slight surface elevations can be observed as wave passes. However, it is difficult to see the difference in wave interactions with original bricks from Figure 13. Further direct comparison is therefore given in Figure 18.

(**a**) Case 1 (A = 0.785 m, T = 4 s) with modified brick.

(**b**) Case 4 (A = 0.755 m, T = 7 s) with modified brick.

Figure 17. Wave interactions with modified brick (**a**) case 1 and (**b**) case 4.

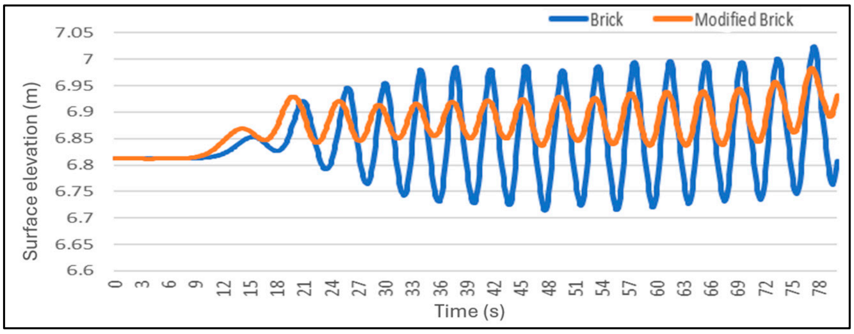

(**a**) Case 1, 5 m behind the OBS (original brick and modified brick)

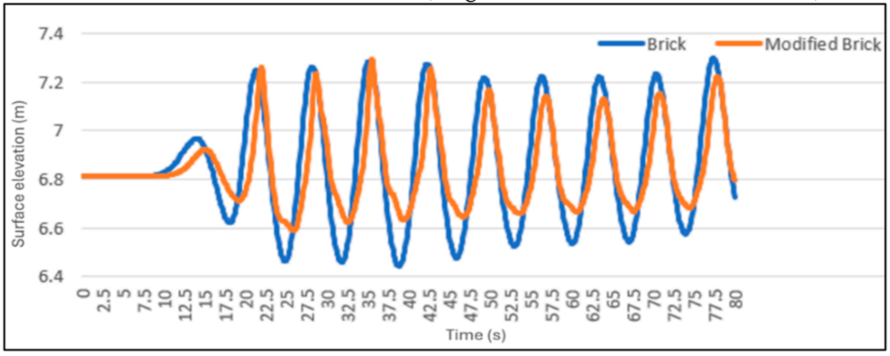

(**b**) Case 4, 5 m behind the OBS (original brick and modified brick)

Figure 18. Surface elevation comparison at 5 m behind the brick.

By comparing the surface elevations, a drastic change in the wave amplitude is observed for case 1, while only a small change is seen for case 4, as shown in Figure 18a,b. A reduction in wave amplitude is evident with the modified brick, indicating that it is effectively dissipates the energy of incoming waves.

Modified brick geometry effectively reduces wave energy, decreasing wave amplitude by 89.2% for case 1, and 55.4% for case 4 as compared to no brick scenario in the NWT. It also outperforms the traditional brick design, offering greater wave attenuation, see Table 6. This improved performance helps further reduce wave amplitude, dissipate wave energy, and enhance the stability of OBS platforms for offshore wind turbine applications.

5. Discussion and Conclusions

In this study, a 3D numerical model is implemented to simulate wave propagation in both linear and nonlinear NWTs that mimic ocean wave behavior. Interactions between waves and the OBS are investigated through numerical analysis. The proposed NWT is verified by comparing the numerical results with the second-order Stokes analytical solution. Validation of the OBS simulation is achieved by comparing the numerical results with experimental data, showing good agreement—particularly in regions of highest pressure.

Comparison of surface elevations demonstrates that the OBS functions as an effective barrier, significantly reducing the amplitude of incoming waves and helping to mitigate coastal erosion. The nonlinear NWT is further used to evaluate a modified OBS design. Moreover, the numerical model is fully utilized by incorporating real-world, full-scale data and applying it in a comprehensive, large-scale NWT simulation. The wave amplitude reduction can reach 70% for a wave with an amplitude of 0.785 m and a period of 5 s.

Results indicate that the modified brick more effectively reduces wave amplitudes and enhances the stability of the OBS in oceanic environments compared to the original design. For the same wave input, the modified brick geometry effectively reduces wave energy, decreasing wave amplitude by 89.2%.

Research is underway, both numerically and experimentally, to further explore the effects of the OBS on wave amplitude reduction. Future work will focus on two main aspects: the influence of geometric parameters and the effects of different wave conditions. For OBS geometric parameters, in the case of the original OBS, we will exam the effect of scaling up the brick size in both simulations and experiments to evaluate its potential for enhancing attenuation of longer wavelengths; for the modified OBS, we will study the impact of thread depth, pitch, and shrinkage ratio on wave attenuation. For wave parameters, we plan to test longer and irregular waves through both numerical simulations and experimental setups.

The current findings of this research are expected to provide valuable insights for continuously improving the design of OBS, enhancing wave attenuation, and increasing the stability of OBS platforms for offshore wind turbine applications.

Author Contributions: Conceptualization, X.W.; methodology, X.W.; software, H.B.; validation, H.B. and J.T.; formal analysis, X.W. and H.B.; experimental testing, data curation, J.T. and H.B.; writing—original draft preparation, H.B.; writing—review and editing, X.W.; visualization, X.W. and H.B.; supervision, X.W. All authors have read and agreed to the published version of the manuscript.

Funding: This research received no external funding.

Data Availability Statement: A thesis work by Hari Bollineni was published in 2024.

Conflicts of Interest: Author Joshua Toblas was employed by the company Ocean Brick System Company. The remaining authors declare that the research was conducted in the absence of any commercial or financial relationships that could be construed as a potential conflict of interest.

References

1. Ocean Brick System. Technology. Available online: https://www.oceanbricks.com/technology (accessed on 2 May 2025).
2. Lopez-Pavon, C.; Souto-Iglesias, A. Hydrodynamic coefficients and pressure loads on heave plates for semi-submersible floating offshore wind turbines: A comparative analysis using large scale models. *Renew. Energy* **2015**, *81*, 864–881. [CrossRef]
3. Shivaji, G.T.; Sen, D. A 3D numerical wave tank study for offshore structures with linear and nonlinear mooring. *Aquat. Procedia* **2015**, *4*, 492–499. [CrossRef]
4. Saincher, S.; Banerjeea, J. Design of a numerical wave tank and wave flume for low steepness waves in deep and intermediate water. *Procedia Eng.* **2015**, *116*, 221–228. [CrossRef]
5. Kim, S.Y.; Kim, K.M.; Park, J.C.; Jeon, G.M.; Chun, H.H. Numerical simulation of wave and current interaction with a fixed offshore substructure. *Int. J. Nav. Archit. Ocean Eng.* **2016**, *8*, 188–197. [CrossRef]
6. Park, J.C.; Kim, M.H.; Miyata, H.; Chun, H.H. Fully nonlinear numerical wave tank (NWT) simulations and wave run-up prediction around 3-D structures. *Ocean Eng.* **2003**, *30*, 1969–1996. [CrossRef]
7. Wang, H.W.; Huang, C.J.; Wu, J. Simulation of a 3D numerical viscous wave tank. *J. Eng. Mech.* **2007**, *133*, 761–772. [CrossRef]
8. Gomes, M.D.N.; Isoldi, L.A.; Olinto, C.R.; Rocha, L.A.O.; Souza, J.A. Computational modeling of a regular wave tank. In Proceedings of the 3rd Southern Conference on Computational Modeling, Rio Grande, Brazil, 23–25 November 2009; IEEE: New York, NY, USA, 2009; pp. 60–65.
9. Liang, X.F.; Yang, J.M.; Li, J.; Xiao, L.F.; Li, X. Numerical simulation of irregular wave-simulating irregular wave train. *J. Hydrodyn.* **2010**, *22*, 537–545. [CrossRef]
10. Li, Z.; Deng, G.; Queutey, P.; Bouscasse, B.; Ducrozet, G.; Gentaz, L.; Le Touzé, D.; Ferrant, P. Comparison of wave modeling methods in CFD solvers for ocean engineering applications. *Ocean Eng.* **2019**, *188*, 106237. [CrossRef]
11. Choi, Y.M.; Kim, Y.J.; Bouscasse, B.; Seng, S.; Gentaz, L.; Ferrant, P. Performance of different techniques of generation and absorption of free-surface waves in Computational Fluid Dynamics. *Ocean Eng.* **2020**, *214*, 107575. [CrossRef]
12. Bihs, H.; Kamath, A.; Chella, M.A.; Aggarwal, A.; Arntsen, Ø.A. A new level set numerical wave tank with improved density interpolation for complex wave hydrodynamics. *Comput. Fluids* **2016**, *140*, 191–208. [CrossRef]
13. Kuai, Y.R.; Zhou, J.F.; Duan, J.L.; Wang, X. Numerical simulation of solitary wave forces on a vertical cylinder on a slope beach. *China Ocean Eng.* **2021**, *35*, 317–331. [CrossRef]
14. Kumar, V.; Bhattacharjee, J. Hydrodynamic Performance of Submerged Breakwaters: An NWT Study. *Ocean Eng.* **2012**, *44*, 23–31.
15. Li, Y.; Lin, M. Wave-current impacts on surface-piercing structure based on a fully nonlinear numerical tank. *J. Hydrodyn. Ser. B* **2015**, *27*, 131–140. [CrossRef]

16. Hu, Z.Z.; Greaves, D.; Raby, A. Numerical wave tank study of extreme waves and wave-structure interaction using OpenFoam®. *Ocean Eng.* **2016**, *126*, 329–342. [CrossRef]
17. Wang, P.; Fang, K.; Wang, G.; Liu, Z.; Sun, J. Experimental and numerical study of the nonlinear evolution of regular waves over a permeable submerged breakwater. *J. Mar. Sci. Eng.* **2023**, *11*, 1610. [CrossRef]
18. Wang, B.; Li, Y.; Wu, F.; Gao, S.; Yan, J. Numerical Investigation of Wave Run-Up and Load on Fixed Truncated Cylinder Subjected to Regular Waves Using OpenFOAM. *Water* **2022**, *14*, 2830. [CrossRef]
19. Akarni, H.; El Aarabi, L.; Mouakkir, L.; Mordane, S. Numerical Modeling of the Wave-Plate-Current Interaction by the Boundary Element Method. *Fluids* **2021**, *6*, 435. [CrossRef]
20. Wang, S.; Liu, S.; Xiang, C.; Li, M.; Yang, Z.; Huang, B. Prediction of Wave Forces on the Box-Girder Superstructure of the Offshore Bridge with the Influence of Floating Breakwater. *J. Mar. Sci. Eng.* **2023**, *11*, 1326. [CrossRef]
21. Tong, C.; Shao, Y.; Bingham, H.B.; Hanssen, F.C.W. An adaptive harmonic polynomial cell method for three-dimensional fully nonlinear wave-structure interaction with immersed boundaries. *Phys. Fluids* **2024**, *36*, 032118. [CrossRef]
22. Liu, S.; Afacan, A.; Masliyah, J. Steady incompressible laminar flow in porous media. *Chem. Eng. Sci.* **1994**, *49*, 3565–3586. [CrossRef]
23. Costa, U.M.S.; Andrade, J.S., Jr.; Makse, H.A.; Stanley, H.E. The role of inertia on fluid flow through disordered porous media. *Phys. A Stat. Mech. Appl.* **1999**, *266*, 420–424. [CrossRef]
24. Macini, P.; Mesini, E.; Viola, R. Laboratory measurements of non-Darcy flow coefficients in natural and artificial unconsolidated porous media. *J. Pet. Sci. Eng.* **2011**, *77*, 365–374. [CrossRef]
25. Horko, M. CFD Optimization of an Oscillating Water Column Energy Converter. Master's Thesis, School of Mechanical Engineering, The University of Western Australia, Perth, Australia, 2007.
26. McCormick, M.E. *Ocean Engineering Mechanics: With Applications*; Cambridge University Press: Cambridge, UK, 2009; p. 55.
27. Hirt, C.W.; Nichols, B.D. Volume of fluid (VOF) method for the dynamics of free boundaries. *J. Comput. Phys.* **1981**, *39*, 201–225. [CrossRef]
28. Menter, F.R. Two-equation eddy-viscosity turbulence models for engineering applications. *AIAA J.* **1994**, *32*, 1598–1605. [CrossRef]
29. Beavers, G.S.; Joseph, D.D. Boundary conditions at a naturally permeable wall. *J. Fluid Mech.* **1967**, *30*, 197–207. [CrossRef]
30. Ujhidy, A.; Nemeth, J.; Szépvölgyi, J. Fluid flow in tubes with helical elements. *Chem. Eng. Process. Process Intensif.* **2003**, *42*, 1–7. [CrossRef]
31. Batchelor, G.K. *An Introduction to Fluid Dynamics*; Cambridge University Press: Cambridge, UK, 1967.